Atomic and electronic structure of Ti substitution in $Ca_3Co_4O_9$

Xuan Hu, Patrick J Phillips, Dipanjan Mazumdar, Juan Carlos Idrobo, Stanislaw Kolesnik, Arunava Gupta, Serdar Ogut, and Robert F. Klie

Citation: J. Appl. Phys. **120**, 205105 (2016); doi: 10.1063/1.4966938
View online: http://dx.doi.org/10.1063/1.4966938
View Table of Contents: http://aip.scitation.org/toc/jap/120/20
Published by the American Institute of Physics

Atomic and electronic structure of Ti substitution in $Ca_3Co_4O_9$

Xuan Hu,[1] Patrick J Phillips,[1] Dipanjan Mazumdar,[2] Juan Carlos Idrobo,[3] Stanislaw Kolesnik,[4] Arunava Gupta,[5] Serdar Ogut,[1] and Robert F. Klie[1]
[1]*Department of Physics, University of Illinois at Chicago, Chicago, Illinois 60607, USA*
[2]*Department of Physics, Southern Illinois University, Carbondale, Illinois 62901, USA*
[3]*Center of Nanophase Materials Sciences, Oak Ridge National Laboratory, Oak Ridge, Tennessee 37830, USA*
[4]*Department of Physics, Northern Illinois University, DeKalb, Illinois 60115, USA*
[5]*Center of Materials for Information Technology, University of Alabama, Tuscaloosa, Alabama 35401, USA*

(Received 8 August 2016; accepted 20 October 2016; published online 29 November 2016)

We examine the role of Ti doping in the incommensurately layered thermoelectric oxide material $Ca_3Co_4O_9$ (CCO). The measured Seebeck coefficient of $S = 135\ \mu V/K$ in Ti-doped CCO thin films of composition $Ca_3Co_{3.8}Ti_{0.2}O_9$ indicates no significant enhancement of S compared to pristine CCO, thus confirming prior experimental results. Using a combination of aberration-corrected scanning transmission electron microscopy, electron energy-loss spectroscopy and first-principles computations, we determine the atomic and electronic structures of Ti-doped CCO, including the preferred location of Ti dopants and valence states of Ti and Co atoms. Our findings on the structural, electronic, and transport properties of the Ti-doped CCO are discussed in light of the previously published results. *Published by AIP Publishing*. [http://dx.doi.org/10.1063/1.4966938]

I. INTRODUCTION

Over the last few decades, the quest for high-efficiency thermoelectric (TE) materials has attracted great attention, since the thermoelectric effect, i.e., direct conversion of heat into electrical energy, is an important method for power generation[1] and electronic refrigeration.[2] As an eco-friendly energy source, the thermoelectric power has the potential to be an alternative to traditional fossil fuels. The efficiency of a thermoelectric material is usually expressed in terms of the dimensionless figure of merit ZT, which is defined as $ZT = \frac{S^2T}{\rho\kappa}$, where S, T, ρ, and κ are Seebeck coefficient, absolute temperature, electrical resistivity, and thermal conductivity, respectively. Large Seebeck coefficient, low electrical resistivity, and low thermal conductivity are required for good TE materials.

While many different material systems have been studied, the class of thermoelectric oxides holds particular promise for achieving high thermal and environmental stability. One class of thermoelectric oxides, the incommensurately layered $Ca_3Co_4O_9$ (CCO), also reported as $[Ca_2CoO_3][CoO_2]_{1.62}$, stands out as a material with a high in-plane Seebeck coefficient,[3–5] high thermoelectric figure of merit ($ZT \sim 1$ at 1000 °C),[6] and high temperature stability. The atomic and electronic properties of pristine CCO have been studied extensively both experimentally and theoretically.[3–26] CCO is made up of two monoclinic subsystems, alternatively stacked along the c-axis: the CdI_2-type CoO_2 layers and the rocksalt (RS) type Ca_2CoO_3 layers. Both subsystems have the same $a = 4.8339$ Å and $c = 10.8436$ Å lattice parameters, but they are incommensurately stacked along the b-axis, with lattice constants of $b = 2.8238$ Å and 4.5582 Å for the CoO_2 and RS subsystems, respectively.[7] Some of us have previously demonstrated that the RS subsystem plays the role of a charge-carrier reservoir, while the CoO_2 layers are p-type conducting.[8]

In strongly correlated oxide materials, such as CCO, the Seebeck coefficient can be determined using the Heikes formula[14]

$$S = -\frac{k_B}{e}\ln\left(\frac{g_3}{g_4}\frac{1-x}{x}\right), \tag{1}$$

where x is the concentration of Co^{4+}, and g_3 and g_4 are the orbital degeneracies of Co^{3+} and Co^{4+} in the CoO_2 layer, respectively. Previous studies have found that the Co^{4+} concentration in the CoO_2 layers is $x = 0.5$, which results in a Co valence state of +3.5.[8,9] Based on Equation (1), we can see that this mixed-valence state in the CoO_2 layer is responsible for the large S (assuming a low spin-state for both the Co^{3+} and Co^{4+} ions) and for the observed p-type conductivity in CCO. However, it can also be seen that at $x = 0.5$, S is limited to 155 μV/K, which has since been confirmed experimentally.[15]

Several studies have suggested various methods to improve the thermoelectric performance of CCO, more specifically the figure of merit, ZT. First, based on Eq. (1), one can increase the Seebeck coefficient by manipulating the orbital degeneracy via a Co-ion spin-state transition. There are several ways to achieve this spin-state transition, including exerting compressive strain on the CoO_2 layer, isovalent doping and defect engineering. For example, recent studies on CCO thin films have shown that the presence of CoO_2 stacking faults could give rise to a Co^{4+} spin-state transition, which stabilizes the Co^{4+} in an intermediate state and increases the Seebeck coefficient.[15,16] However, the application of bi-axial strain using a lattice mismatch between the substrate and the single crystal CCO films has proven to be less successful.[16]

Second, one can increase the Seebeck coefficient by increasing the Co^{4+} concentration x, i.e., increasing the valence state of Co in the CoO_2 layer. Doping the Ca, or the Co sites in both subsystems, is a possible approach to influence the valence state of Co in the CoO_2 layer and improve the TE properties of CCO.[10–13,19–22,24] Since Co atoms play a key role in the electronic and thermal properties of CCO, doping on the

Co sites is more likely to have a significant influence on the electronic and thermal properties.[10–13,24] To minimize the structural changes while maintaining a high doping concentration, the ionic size of the dopants on the Co sites should be similar to that of Co, which limits the possible dopants to the transition metals from Ti to Zn in the periodic table. For instance, one study has reported that Fe dopants at the Co sites of CCO increase the Seebeck coefficient and decrease the electronic resistivity simultaneously.[23] Similarly, another study has shown that the Fe and Mn substitution of Co atoms in the CoO_2 layer enhance the electronic correlations in the system, while the Cu substitution of Co in the RS layer does not affect the electronic and magnetic properties.[19]

In a recent study by Xu *et al.*,[25] it was suggested that the Ti dopants introduce a significant increase in the Seebeck coefficient. The authors proposed that when the concentration of Ti dopants is less than $x = 0.2$ for $Ca_3Co_{4-x}Ti_x O_9$, Ti atoms mainly replace Co atoms in the RS subsystem, while, as x approaches 0.3, Ti dopants start to substitute Co atoms in both subsystems. The authors found that when Ti replaces Co in the CoO_2 layer, the Seebeck coefficient increases from 130 μV/K to above 175 μV/K.[27] However, a more recent study on Ti-doped CCO by Torres *et al.* showed that while Ti substitution results in a decrease of electrical resistivity, there is no appreciable change in the Seebeck coefficient.[26] It should be noted that these doping studies have been conducted on polycrystalline bulk samples without a comprehensive understanding of Ti dopant effects on the local atomic and electronic structures.

In this paper, we use a combined experimental and theoretical approach to determine the effects of Ti doping on the structural and electronic properties of CCO. More specifically, we combine the aberration-corrected scanning transmission electron microscopy (STEM), electron energy-loss spectroscopy (EELS), first-principles density functional theory (DFT), and pulsed-laser deposition (PLD) thin-film synthesis to study the structure and transport properties of Ti-doped CCO. We find that for 100 nm thick films grown on $SrTiO_3$ [001], there is no difference in the Seebeck coefficients of Ti-doped and pristine CCO.[16] We determine the structure of Ti-doped CCO both experimentally and theoretically, and find that Ti doping has very little effect on either the local atomic structure or the density of states (DOS) of Co in the CoO_2 subsystem. The rest of the paper is organized as follows: In Sec. II, we provide the details of experimental and computational methods. The structure of Ti-doped CCO and the position of the Ti dopants are discussed in Sec. III. In Sec. IV, we present EELS and DFT studies for the electronic structure of Ti-doped CCO. Finally, in Sec. V, we discuss and summarize our findings in light of the previously published results.

II. METHODS

A. Experimental methods

Ti-doped CCO thin films ($Ca_3Co_{3.8}Ti_{0.2}O_9$) were deposited by PLD with a Coherent Lambda Physik Excimer laser ($\lambda = 248$ nm, repetition rate is between 4 and 8 Hz). The films were 100 nm thick and grown on a (001)-oriented $SrTiO_3$ substrate. The optimal condition was found with laser fluence at 1.5 J/cm^2 and oxygen pressure at 300 mTorr. More details on the thin film synthesis of CCO can be found in Ref. 16. All atomic-resolution STEM images presented here were acquired on a Nion UltraSTEM at Oak Ridge National Laboratory, operated at 100 kV. The semi-convergence angle for the high-angle annular dark field (HAADF) imaging was chosen to be 30 mrad, which results in an image intensity proportional to approximately Z^2.[28–30] To analyse the influence on the electronic structure, the EEL spectra were acquired with a dispersion of 0.5 eV per channel to record the O *K*-, Ti *L*-, and Co *L*-edges simultaneously. The Seebeck coefficient was measured by using a physical property measurement system (Quantum Design) equipped with a thermal transport option.[16]

B. Computational methods

First-principles calculations within the framework of density functional theory (DFT) were carried out using the Perdew-Burke-Ernzerhof (PBE)[31,32] exchange correlation functional and the plane-wave pseudopotential method as implemented in the Vienna *Ab Initio* Simulation Package (VASP).[33] Rébola *et al.*[17,18] suggested that the incommensurately layered CCO can be modeled using rational approximants of composition $[Ca_2CoO_3]_{2F(n)}[CoO_2]_{2F(n+1)}$, where $F(n)$ are Fibonacci numbers. Their study showed that the 5/3 approximant, which leads to a composition of $[Ca_2CoO_3]_6[CoO_2]_{10}$ with 66 atoms in the unit cell, does a good job in modeling the essential electronic properties of CCO. Here, we used the same 5/3 unit cell for all the calculations and tested some of our results using a smaller unit cell of composition $[Ca_2CoO_3]_4[CoO_2]_6$ (i.e., the 3/2 approximant). The plane wave cutoff energy was 550 eV. $6 \times 3 \times 3$ Monkhorst-Pack k-point mesh was used for the 5/3 unit cells. To model the moderate electronic correlations in CCO, our calculations were performed within the PBE+U framework, where we used an onsite effective Coulomb interaction of $U - J = 4$ eV. For Ti-doped CCO, we tested the $U - J$ values ranging from 0 to 4 eV on the Ti atom. Different effective U values resulted in essentially the same characteristics in the density of states. Therefore, we chose an effective $U = 0$ eV on the Ti atom for simplicity. Defect formation energies were computed as a function of the chemical potentials μ_i (i = Ti, Co, Ca, O) using well-established methods with grand canonical ensembles.[34–36] The boundaries of the individual chemical potentials were determined by using equilibrium with bulk CCO and by avoiding precipitation of secondary phases such as bulk Ca, CaO, Co, CoO, Co_3O_4, Ti, Ti_2O, TiO, Ti_2O_3, TiO_2, $CaTiO_3$ compounds and molecular oxygen.

III. STRUCTURAL PROPERTIES OF Ti-DOPED CCO

Fig. 1 shows HAADF images of the pristine CCO and the nominally 100 nm thick Ti-doped CCO ($Ca_3Co_{3.8}Ti_{0.2}O_9$) single crystal film in the [110] projection. The layered structure of CCO includes the Ca_2CoO_3 subsystem with the RS structure and the CdI_2-type layers of the CoO_2 subsystem. These two sub-systems are stacked alternatively along the c-axis. Comparing the Z-contrast images for pristine and the Ti-doped CCO, we find that there is no apparent change in the

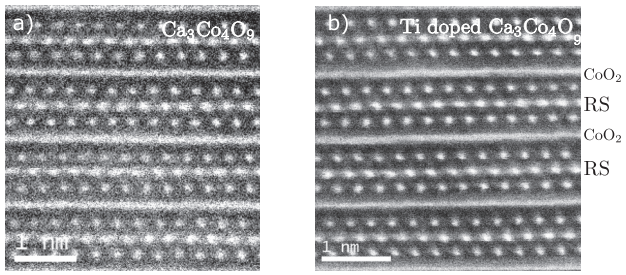

FIG. 1. High-angle annular dark field (HAADF) images of (a) the pristine CCO thin film and (b) the Ti-doped CCO thin film both in the [110] projection.

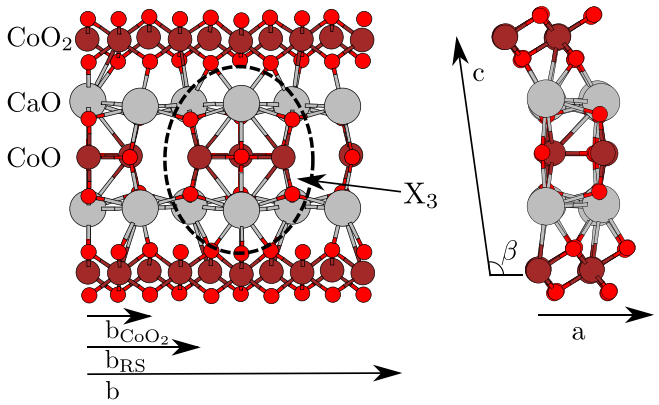

FIG. 2. Relaxed structures of pristine CCO with a 5/3 approximant unit cell along the [100] (left) and [010] (right) directions. The grey, red, and dark red balls represent Ca, O, and Co atoms, respectively. The clustering with three units of Ca_2CoO_3 (X_3) in the RS subsystem is highlighted with a dashed ellipse. The lattice constants along the *b*-axis for the RS and CoO_2 subsystems (b_{RS} and b_{CoO_2}) are also shown.

crystal structure upon doping with Ti, which suggests that the Ti dopants do not influence the atomic structure significantly.

In order to investigate this further, we performed the first-principles calculations on the structure of the pristine and Ti-doped CCO. The optimized structure of pristine CCO with a 5/3 unit cell is shown in Fig. 2. After structural relaxation, we find a clustering with three units of Ca_2CoO_3 (denoted by X_3) along the *b* axis of the RS subsystem, which is a feature also observed by Rébola *et al.*[17] Due to this clustering, the CoO_6 octahedra on the either side of X_3 are significantly distorted. The lattice parameters of the optimized structure with the 5/3 unit cell are shown in Table I. The results are essentially the same as those obtained by Rébola *et al.*[17] and agree well with the experimental data.[7]

Next, we studied Ti dopants by substituting Ti for Co atoms (in the RS or CoO_2 layer) or Ca atoms. All 16 Co sites and 12 Ca sites in the 5/3 unit cell have been considered. The optimized structures with Ti substitution at four

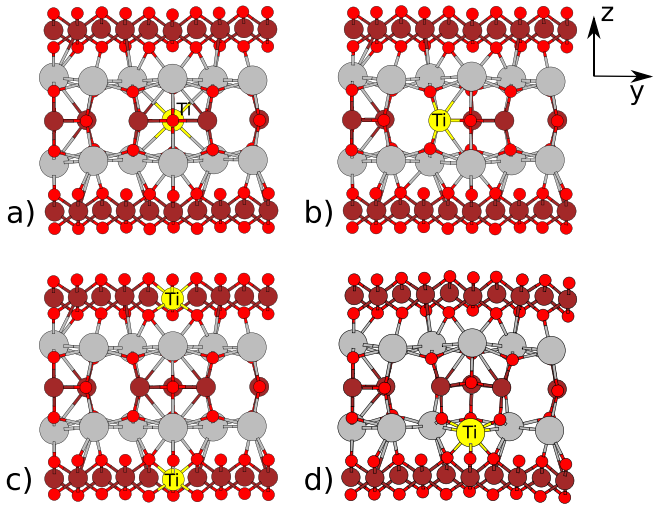

FIG. 3. Optimized structures of Ti-doped CCO with Ti atom at (a) the Co site in the middle of the X_3 cluster, (b) the Co site on the side of the X_3 cluster, (c) the Co site in the CoO_2 layer, (d) the Ca site in RS. The yellow balls represent the Ti atoms.

inequivalent sites are presented in Fig. 3. By comparing the optimized structures of Ti-doped CCO with that of pristine CCO, we find that the average Ti-O bond lengths differ from the original Co-O bond lengths by only 1.6%, −3.1%, and 3.1%, when the Ti substitutes the Co atom (i) in the middle of X_3, (ii) on the side of X_3, and (iii) in the CoO_2 layer, respectively. When Ti substitutes a Ca atom, on the other hand, the percentage difference of the average Ti-O bond length from the original Ca-O bond length is found to be −17.8%. This shows that the structural changes induced by Ti substitution at Co sites are relatively small, while the Ti doping at a Ca site results in a significant reduction of bond length between the central ion and the ligands. This reduction of bond length is due to the more attractive potential caused by the additional positive charge of a Ti ion (4+) compared to a Ca ion (2+). These calculations along with the HAADF images (shown in Fig. 1) suggest that Ti substitutes Co rather than Ca atoms, since the latter scenario would imply significant structural rearrangements not observed experimentally. However, this analysis does not provide sufficient insight to distinguish between Ti-doping at the RS or the CoO_2 subsystems, which we investigate next.

In order to determine the location of Ti dopants, we have performed atomic-resolution EELS measurements. Figures 4(a)–4(d) shows the Z-contrast and EEL spectrum images of CCO, including the integrated Co, Ti, and Ca *L*-edge intensity distributions. Fig. 4(e) shows the profile of the Ti *L*-edge intensity integrated along the *c* axis. The integrated signal of Ti *L*-edge shows the relative concentration

TABLE I. Calculated lattice parameters (in Å) for the 5/3 approximant of bulk CCO compared with previous calculations of Rébola *et al.*[17] and experimental data taken from Ref. 7. b_{RS} and b_{CoO_2} are the lattice constants along the *b*-axis for the RS and CoO_2 subsystems, respectively.

System	*a*	b_{RS}	b_{CoO_2}	*c*	*β*
5/3 (This work)	4.87	4.70	2.81	10.85	98.37°
5/3 (Rébola *et al.*[17])	4.88	4.71	2.82	10.85	98.34°
Experiments (Miyazaki *et al.*[7])	4.83	4.56	2.82	10.84	98.13°

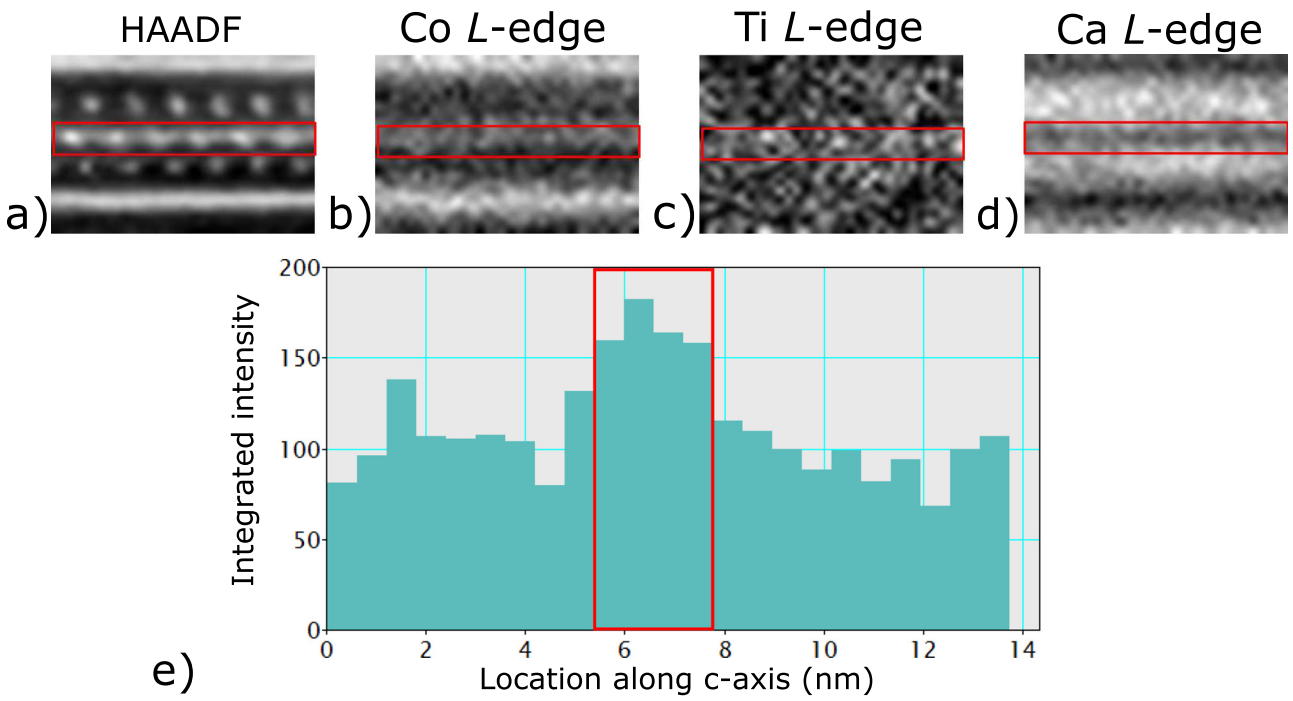

FIG. 4. The Z-contrast (a) and EEL spectrum images (b)–(d) of CCO showing the integrated Co, Ti, and Ca *L*-edge distributions. The integrated Ti *L*-edge signal is shown in (e). Here, the Ti *L*-edge intensity is integrated horizontally across the entire spectrum image shown in (c). The red rectangular region corresponds to the CoO layer of the RS subsystem.

of the Ti dopants. We find that the Ti signal reaches its maximum at the CoO column of the RS subsystem. This implies that the Ti dopants mostly replace Co in the CoO column of the RS subsystem.

To gain further insight about the location of Ti dopants, we used first-principles calculations to determine the formation energies of Ti_{Co} (Ti atom substituting a Co atom in either the RS or CoO_2 layer) and Ti_{Ca} (Ti substituting a Ca atom) as a function of the individual chemical potentials μ_i ($i =$ Ti, Co, Ca). The computed formation energies with a 5/3 unit cell (averaged over all possible locations) in the Ti-rich region (with μ_{Ti} achieving its maximum value) are 0.09, 0.22, and 2.07 eV for Ti_{Co} (RS layer), Ti_{Co} (CoO_2 layer), and Ti_{Ca}, respectively (shown in Table II).[37] This shows a strong preference of Ti atoms substituting for Co, rather than Ca atoms. This also shows a somewhat significant (by 0.13 eV) preference for Ti substituting Co atoms in the RS subsystem, rather than the CoO_2 subsystem, in agreement with our findings based on the EELS analysis.

We also computed the formation energies of Ti defects using a 3/2 unit cell of CCO (shown in Table II). In this case, the averaged formation energies for Ti_{Co} (RS layer), Ti_{Co} (CoO_2 layer), and Ti_{Ca} are −0.06, 0.60, and 1.91 eV, respectively, which indicates an even stronger preference (by 0.66 eV) for Ti to substitute a Co atom in the RS subsystem. In our calculations, Ti defects were simulated by substituting one atom (Co or Ca) at a time in the pristine unit cell. The compositions of Ti-doped (at a Co site) unit cells are therefore, $Ca_{12}Co_{15}TiO_{38}$ and $Ca_8Co_9TiO_{24}$ for the 5/3 and 3/2 unit cells, respectively. The differences in the formation energies are most likely due to the different doping rates and the different in-plane strain between the two misfit subsystems. Irrespective of the structural models, our results show that (1) Ti dopants tend to substitute Co atoms rather than Ca atoms, and (2) Ti dopants are more likely to replace Co atoms in the RS rather than the CoO_2 subsystem.

TABLE II. The formation energies for Ti substitution on the Co sites in both sub-systems and the Ca sites. The formation energies are given for the 5/3 and 3/2 approximants in units of eV.

System	Ti_{Co} (RS layer)	Ti_{Co} (CoO_2 layer)	Ti_{Ca}
5/3 unit cell	0.09	0.22	2.07
3/2 unit cell	−0.06	0.60	1.91

IV. ELECTRONIC PROPERTIES OF Ti-DOPED CCO

The Seebeck coefficient of our Ti-doped thin-film CCO was measured to be $S = 135\,\mu$V/K at room temperature. Therefore, we find no significant enhancement of S compared to pristine bulk CCO ($S \approx 130\,\mu$V/K) within the experimental uncertainty of our transport measurement.[27] In order to explain this phenomenon and examine the electronic properties of Ti-doped CCO, we compare the near-edge fine-structures of the Ti *L*-, Co *L*-, and O *K*-edges with the corresponding density of states (DOS) from our DFT calculations.

To study the valence state of Ti, the fine-structure of the Ti *L*-edge was analysed. Fig. 5 shows the near-edge fine-structure of the Ti *L*-edge in Ti-doped CCO, representing the excitation of $2p$ electrons into the unoccupied $3d$ orbitals. The Ti *L*-edge onset energy was found to be 460.5 eV, when the spectrum is calibrated with respect to

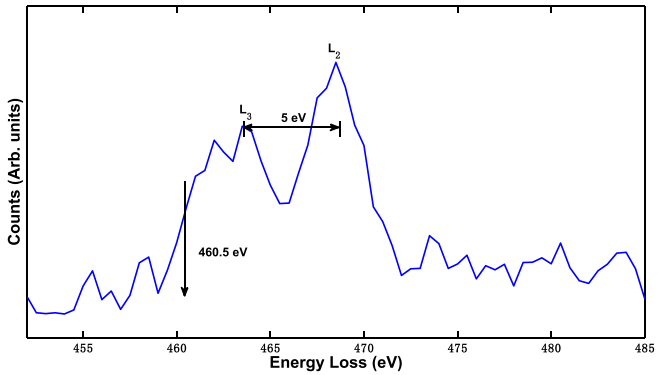

FIG. 5. The EEL spectra of Ti *L*-edge in Ti-doped CCO. The spectra are calibrated with respect to O *K*-edge onset at 532 eV. The split and onset of $L_{2,3}$ edge are 5.0 eV and 460.5 eV, respectively.

the O *K*-edge onset at 532 eV. The splitting of the Ti L_3 and L_2 edges was measured as 5.0 eV. Using the previously published relationship between the Ti *L*-edge onset and the Ti valence state,[38] we find that Ti is in a 4+ valence state in our doped CCO thin films. More specifically, our measured Ti *L*-edge onset and L_3–L_2 splitting are very close to the corresponding values of 459.5 eV and 4.8 eV, respectively, measured by Sankararaman and Perry[39] for Ti^{4+}.

To further study the occupancy of Ti 3*d* orbitals, we have calculated and analyzed the projected density of states (DOS). Figs. 6(a) and 6(b) show the projected DOS of Ti *d*-orbitals when Ti substitutes Co in the CoO_2 and the RS subsystems, respectively. In both cases, we observe that the Ti t_{2g} (d_{xy}, d_{yz}, d_{xz}) and e_g (d_{z^2}, $d_{x^2-y^2}$) orbitals are unoccupied. We note that for the case of Ti in the CoO_2 layer, the coordination of Ti with oxygen is nearly perfectly octahedral. As a result, the orbitals within the t_{2g} and e_g manifolds remain degenerated in both spin channels. However, for Ti in the RS subsystem, the TiO_6 octahedra are compressed along the *c*-axis, which causes splittings in the two manifolds, which is particularly noticeable for e_g orbitals, as shown in Figure 6(b). The partial DOS below the Fermi-level, which results from the covalent bonding between the O 2*p* and the Ti 3*d* orbitals, is negligible. Therefore, we find the Ti atom to be in a 4+ charge state ($t_{2g}^0 e_g^0$) for Ti substituting Co either in the RS or the CoO_2 subsystems, which agrees with the experimental findings based on the Ti *L*-edge analysis.

Next, we study the valence state of Co upon Ti-doping. Fig. 7 shows the projected DOS for the *d*-orbitals of Co in the CoO_2 layer before and after the Ti substitution of Co in the RS subsystem (the results for Ti_{Co} when Ti substitutes Co in the CoO_2 layer are the same). The t_{2g}–e_g splitting due to the ligand field in the CoO_6 octahedra is clearly visible. While the e_g orbitals are all unoccupied, the t_{2g} orbitals are mostly occupied except for a small region of up to 0.2 eV above the Fermi level in the spin-up channel. That the t_{2g}

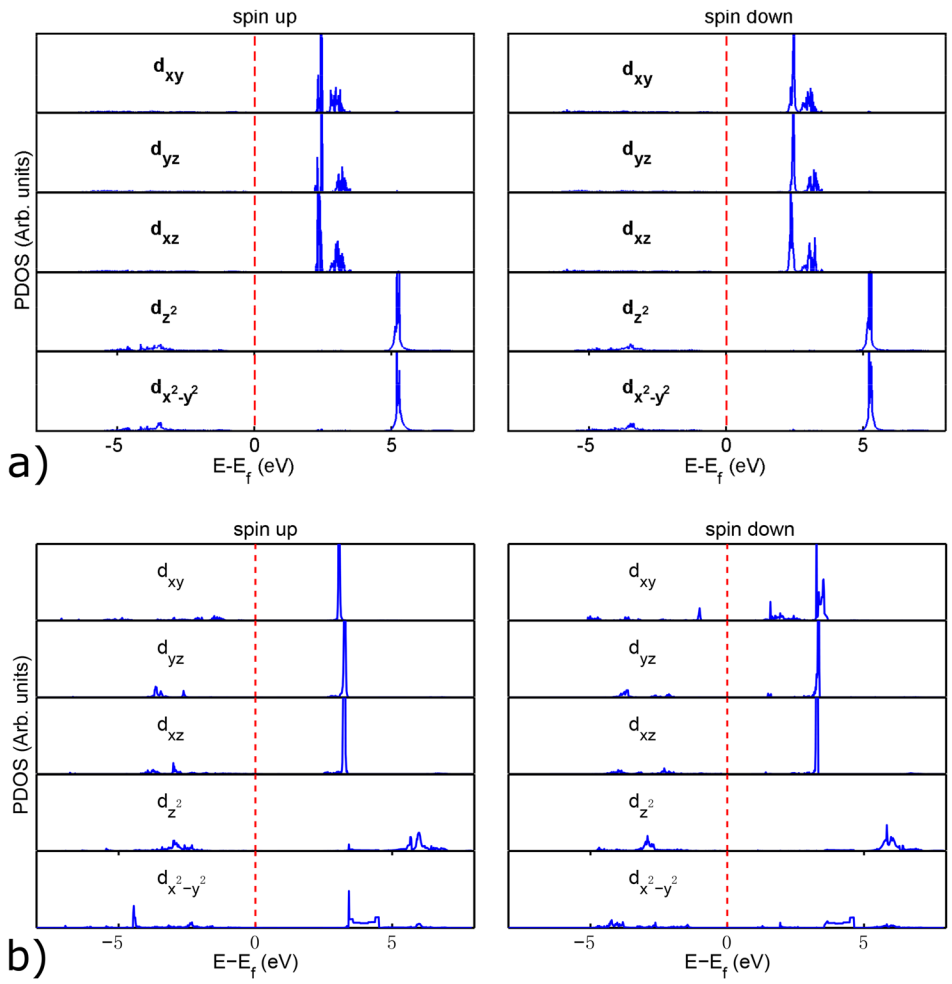

FIG. 6. Partial DOS projected into angular momentum resolved *d* orbitals of Ti atoms when Ti substitutes a Co atom in (a) the CoO_2 layer, and (b) the RS subsystem.

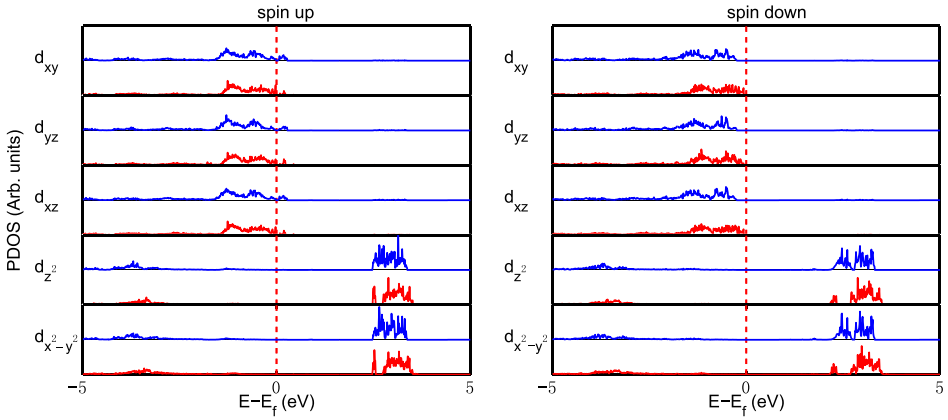

FIG. 7. Partial DOS projected into angular momentum resolved *d* orbitals of Co (in the CoO_2 layer) before (blue curves, upper panel of each angular momentum component) and after (red curves, lower panel of each angular momentum component) the Ti substitution of a Co atom in the RS subsystem.

orbitals are not fully occupied implies that Co is in a mixed valence state of Co^{3+} ($t_{2g}^6 e_g^0$) and Co^{4+} ($t_{2g}^5 e_g^0$). After Ti substitution, the ratio of unoccupied to occupied t_{2g} orbitals remains the same, which indicates that the Co valence state is not affected by the Ti substitution.

To further investigate the influence of Ti dopants on the electronic structure of Co, we can analyze the change of the experimentally measured Co *L*-edges as a function of Ti concentration. Since Ti does not replace Ca atoms (as discussed in Sec. III), we use the Ti/Ca intensity-ratio as a measurement of the local Ti concentration. We find that even within the same sample, the Ti/Ca intensity ratio exhibits an inhomogeneity within the range of 0.067 (±0.01)–0.130 (±0.02). Fig. 8(a) shows the EEL spectra of Co *L*-edges in the CoO_2 layer for two different Ti concentrations (corresponding to Ti/Ca intensity ratios of 0.067 and 0.130). The two signals are normalized with respect to a 50 eV window (830 eV–880 eV) above the Co L_2 edge. We find that there is no difference between these two signals in terms of their edge onsets and the $L_{3,2}$ splitting, even though one spectrum is taken from a region with twice the Ti concentration. Fig. 8(b) shows the Co L_3/L_2 ratio as a function of the Ti concentration, and we can clearly see that there is no significant correlation between the Ti concentration and the Co $L_{2,3}$ ratio with almost all the measured values corresponding to a Co valence of 3.5+ (within the experimental error bars) as in pristine CCO. This is in agreement with the results from DOS analysis discussed above.

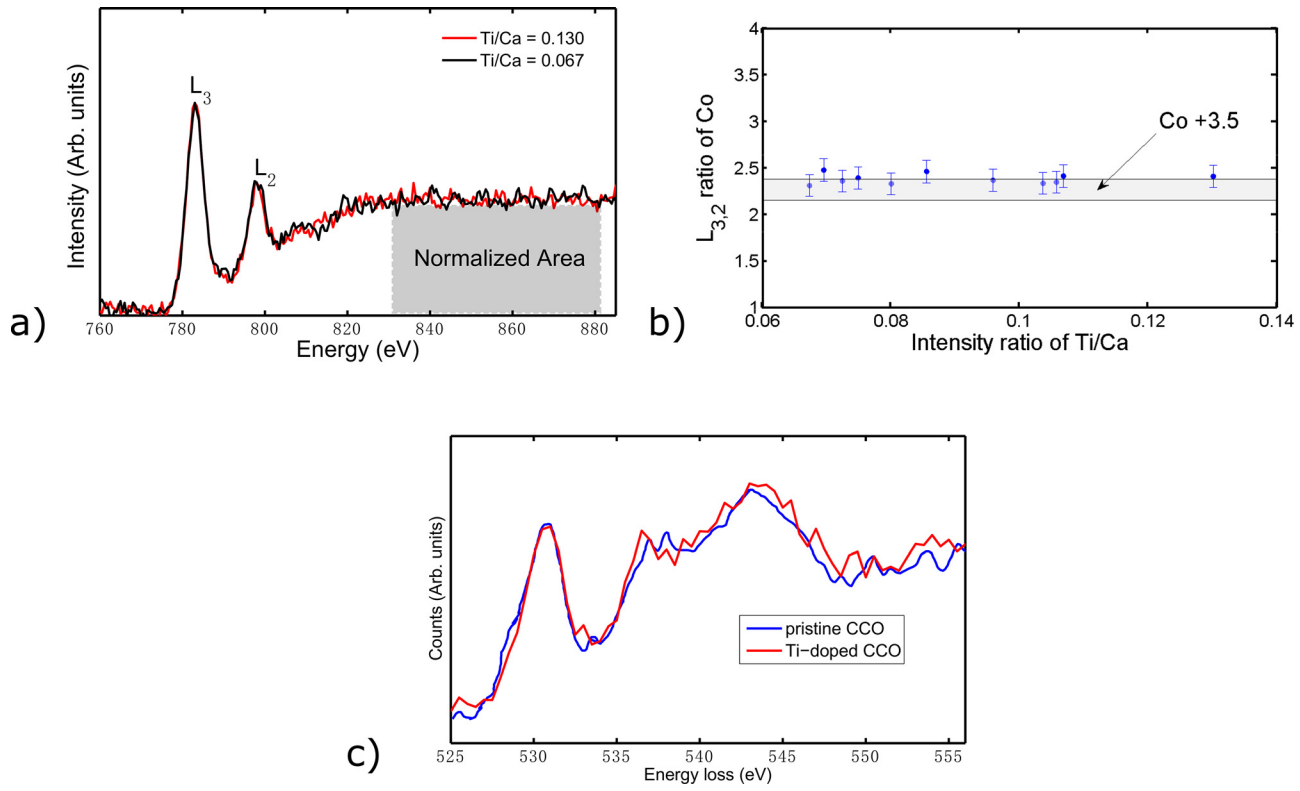

FIG. 8. (a) EEL spectra of Co *L*-edges taken from regions with two different Ti concentrations corresponding to Ti/Ca intensity ratios of 0.067 and 0.13. (b) Co L_3/L_2 ratio as a function of the Ti concentration. The shaded grey area corresponds to a Co valence of 3.5+ with a 5% error bar. (c) EEL spectra of O K-edge of O column in the CoO_2 layer for the pristine and Ti-doped CCO.

Finally, we examine the O *K*-edge fine-structure. As previously shown, the O *K*-edge pre-peak is correlated to the hole concentration and the Co-ion spin state.[15,40] Fig. 8(c) shows the O *K*-edge taken from the CoO_2 layers for the pristine and Ti-doped CCO. Within the experimental error bars, we do not observe a systematic change in the O *K*-edge fine-structure, either, which further confirms that the Co valence and spin-states remain unchanged after Ti-doping.

V. DISCUSSION AND SUMMARY

In this paper, we have examined the structural, electronic, and transport properties of Ti-doped CCO thin films using a combination of first-principles modeling and atomic-resolution scanning transmission electron microscopy. From both Z-contrast imaging and structural optimization studies, we do not find any appreciable change in the crystal and local atomic structures upon Ti doping. The EEL spectra of Ti, Ca, and Co *L*-edge distributions strongly suggest that Ti replaces Co in the RS sub-system. This experimental result is confirmed by our first-principles calculations, which find the lowest formation energy for Ti_{Co}-type defects when Ti substitutes the Co atoms in the RS layers. Furthermore, from an analysis of the site-projected partial density of states, as well as the EELS fine-structure studies, we find the Co and Ti valence states to be +3.5 and +4, respectively. This implies that there is no change in the Co valence state, the Co-ion spin state, or the overall charge carrier concentration in the *p*-type CoO_2-layers compared to pristine CCO. All of these results are consistent with our finding of no enhancement in the Seebeck coefficient for Ti-doped CCO samples in comparison to pristine CCO.

While the preferential location of Ti dopants (in the RS sub-system), as predicted by our first-principles calculations, agrees with the earlier experimental results by Hu *et al.*,[27] our measured Seebeck coefficient of 135 μV/K is significantly lower than the value of 175 μV/K reported in that study. On the other hand, our measured Seebeck coefficient is consistent with the values measured by Torres *et al.*,[26] who found no enhancement in the Seebeck coefficient for Ti-doping concentrations of up to $x = 0.07$ in $Ca_3Co_{4-x}Ti_xO_9$. Another study of Ti-doped single crystal CCO with doping concentrations up to $x = 0.8$, did not find any significant improvement in the in-plane Seebeck coefficient at room temperature and doping concentrations as high as $x = 0.6$ beyond the previously reported bulk values ($S_{ab} \approx 135$ μV/K).[10] In our studies, the Ti doping concentration was fixed at $x = 0.2$ (experiments) and $x = 0.25$ (calculations). It is perhaps possible that relatively higher doping concentrations (i.e., $x \geq 0.3$) may influence the Seebeck coefficient as suggested by Xu *et al.* and our current study cannot rule out this effect. Therefore, higher doping concentration studies in thin films are needed to develop a more comprehensive understanding of the Ti doping effects on the transport properties of CCO.

ACKNOWLEDGMENTS

X.H. and R.F.K. acknowledge support from the National Science Foundation (Grant No DMR-1408427). Electron microscopy research was conducted as part of a user project through Oak Ridge National Laboratory's Center for Nanophase Materials Sciences (CNMS), which is a U.S. Department of Energy Office of Science User Facility.

This research used resources of the National Energy Research Scientific Computing Center, a DOE Office of Science User Facility supported by the Office of Science of the U.S. Department of Energy under Contract No. DE-AC02-05CH11231 (X.H., S.O.).

[1] J. Yang and T. Caillat, MRS Bull. **31**, 224 (2006).
[2] R. Taylor and G. Solbrekken, IEEE Trans. Compon. Packag. Technol. **31**, 23 (2008).
[3] A. C. Masset, C. Michel, A. Maignan, M. Hervieu, O. Toulemonde, F. Studer, B. Raveau, and J. Hejtmanek, Phys. Rev. B **62**, 166 (2000).
[4] P. Limelette, V. Hardy, P. Auban-Senzier, D. Jérome, D. Flahaut, S. Hébert, R. Frésard, C. Simon, J. Noudem, and A. Maignan, Phys. Rev. B **71**, 233108 (2005).
[5] D. Flahaut, T. Mihara, R. Funahashi, N. Nabeshima, K. Lee, H. Ohta, and K. Koumoto, J. Appl. Phys. **100**, 084911 (2006).
[6] M. Shikano and R. Funahashi, Appl. Phys. Lett. **82**, 1851 (2003).
[7] Y. Miyazaki, M. Onoda, T. Oku, M. Kikuchi, Y. Ishii, Y. Ono, Y. Morii, and T. Kajitani, J. Phys. Soc. Jpn. **71**, 491 (2002).
[8] G. Yang, Q. Ramasse, and R. F. Klie, Phys. Rev. B **78**, 153109 (2008).
[9] G. Yang, Q. Ramasse, and R. F. Klie, Appl. Phys. Lett. **94**, 093112 (2009).
[10] B. C. Zhao, Y. P. Sun, W. J. Lu, X. B. Zhu, and W. H. Song, Phys. Rev. B **74**, 144417 (2006).
[11] B. C. Zhao, Y. P. Sun, and W. H. Song, J. Appl. Phys. **99**, 073906 (2006).
[12] I. Matsubara, R. Funahashi, M. Shikano, K. Sasaki, and H. Enomoto, Appl. Phys. Lett. **80**, 4729 (2002).
[13] G. Xu, R. Funahashi, M. Shikano, I. Matsubara, and Y. Zhou, Appl. Phys. Lett. **80**, 3760 (2002).
[14] W. Koshibae, K. Tsutsui, and S. Maekawa, Phys. Rev. B **62**, 6869 (2000).
[15] R. F. Klie, Q. Qiao, T. Paulauskas, A. Gulec, A. Rébola, S. Öğüt, M. P. Prange, J. C. Idrobo, S. T. Pantelides, S. Kolesnik, B. Dabrowski, M. Ozdemir, C. Boyraz, D. Mazumdar, and A. Gupta, Phys. Rev. Lett. **108**, 196601 (2012).
[16] Q. Qiao, A. Gulec, T. Paulauskas, S. Kolesnik, B. Dabrowski, M. Ozdemir, C. Boyraz, D. Mazumdar, A. Gupta, and R. F. Klie, J. Phys.: Condens. Matter **23**, 305005 (2011).
[17] A. Rébola, R. F. Klie, P. Zapol, and S. Öğüt, Phys. Rev. B **85**, 155132 (2012).
[18] A. Rébola, R. F. Klie, P. Zapol, and S. Öğüt, Appl. Phys. Lett. **104**, 251910 (2014).
[19] Y. Wang, Y. Sui, P. Ren, L. Wang, X. Wang, W. Su, and H. Fan, Chem. Mater. **22**, 1155 (2010).
[20] S. Altin, A. Bayri, S. Demirel, and M. Aksan, Curr. Appl. Phys. **14**, 590 (2014).
[21] Y. Fu, S. Lin, Y. Huang, R. Shi, and B. Zhao, J. Alloys Compd. **613**, 87 (2014).
[22] Q. Yao, D. L. Wang, L. D. Chen, X. Shi, and M. Zhou, J. Appl. Phys. **97**, 103905 (2005).
[23] C. J. Liu, L. C. Huang, and J. S. Wang, Appl. Phys. Lett. **89**, 204102 (2006).
[24] P. Srepusharawoot, S. Pinitsoontorn, and S. Maensiri, Comput. Mater. Sci. **114**, 64 (2016).
[25] L. Xu, F. Li, and Y. Wang, J. Alloys Compd. **501**, 115 (2010).
[26] M. Torres, S. Rasekh, P. Bosque, G. Constantinescu, M. Madre, J. Diez, and A. Sotelo, J. Mater. Sci.: Mater. Electron. **26**, 815 (2015).
[27] Y. F. Hu, E. Sutter, W. D. Si, and Q. Li, Appl. Phys. Lett. **87**, 171912 (2005).
[28] A. V. Crewe, J. Wall, and J. Langmore, Science **168**, 1338 (1970).
[29] S. Pennycook and D. Jesson, Ultramicroscopy **37**, 14 (1991).
[30] O. L. Krivanek, M. F. Chisholm, V. Nicolosi, T. J. Pennycook, G. J. Corbin, N. Dellby, M. F. Murfitt, C. S. Own, Z. S. Szilagyi, M. P. Oxley, S. T. Pantelides, and S. J. Pennycook, Nature **464**, 571 (2010).
[31] J. P. Perdew and A. Zunger, Phys. Rev. B **23**, 5048 (1981).
[32] J. P. Perdew, K. Burke, and M. Ernzerhof, Phys. Rev. Lett. **77**, 3865 (1996).
[33] G. Kresse and J. Hafner, Phys. Rev. B **47**, 558 (1993).
[34] S. B. Zhang, J. Phys.: Condens. Matter **14**, R881 (2002).
[35] C. G. Van de Walle and J. Neugebauer, J. Appl. Phys. **95**, 3851 (2004).
[36] C. S. Hellberg, K. E. Andersen, H. Li, P. J. Ryan, and J. C. Woicik, Phys. Rev. Lett. **108**, 166101 (2012).
[37] In principle, the formation energy of a defect will depend on the individual chemical potentials. However, the constraint imposed by

the condition of avoiding precipitation of bulk CoO, Co_3O_4, and $CaTiO_3$ forces the μ_{Ti} to attain its maximum value which also fixes the chemical potentials μ_{Ca}, μCo, and μ_O. The formation energies given in the text correspond to this particular point in the ternary phase diagram.

[38]A. Ohtomo, D. A. Muller, J. L. Grazul, and H. Y. Hwang, Nature **419**, 378 (2002).
[39]M. Sankararaman and D. Perry, J. Mater. Sci. **27**, 2731 (1992).
[40]R. F. Klie, J. C. Zheng, Y. Zhu, M. Varela, J. Wu, and C. Leighton, Phys. Rev. Lett. **99**, 047203 (2007).